Physics of the Earth and Planetary Interiors 262 (2017) 1–7

Contents lists available at ScienceDirect

Physics of the Earth and Planetary Interiors

journal homepage: www.elsevier.com/locate/pepi

Inversion of the moment-tensor M_{rr} components of the 2012 Sumatra strike-slip double earthquake using radial normal modes

Eliška Zábranová *, Ctirad Matyska

Department of Geophysics, Faculty of Mathematics and Physics, Charles University, V Holešovičkách 2, CZ-18000 Prague, Czech Republic

ARTICLE INFO

Article history:
Received 28 June 2016
Received in revised form 3 October 2016
Accepted 7 October 2016
Available online 15 October 2016

Keywords:
2012 Sumatra earthquakes
Superconducting-gravimeter data
Radial modes
CMT inversion

ABSTRACT

On April 11, 2012, two strike-slip Sumatra earthquakes with moment magnitudes higher than 8 generated strong, preferentially horizontal, motions. If only body and surface waves are inverted, their centroid-moment-tensor (CMT) parameters producing vertical motions, in particular the M_{rr} components, are poorly resolved. Independent constraints can be obtained from observations of the radial free-oscillation modes. The signal of radial modes is acquired from four unperturbed superconducting gravimeter records with low noise levels in submillihertz frequency range. We show that the observed signal substantially differs from the synthetic calculations for most of the published CMTs except for the Global CMT solution, which agrees better. We perform modal inversions considering uncertainties in centroid times and calculate marginal posterior probability density function of the M_{rr} components. The amplitude-spectrum inversion is robust enough to estimate the intervals of admissible M_{rr} values. Finally, we incorporate also a phase information and reduce the trade-off between the M_{rr} components of the two studied events.

1. Introduction

Two strike-slip earthquakes with moment magnitudes higher than 8 occurred off the west coast of the northern Sumatra on April 11, 2012, Fig. 1, where faults within the oceanic lithosphere of the Indo-Australia plate were activated. Tectonic explanation of such large unprecedented strike-slip intraplate earthquakes is rather complicated. Delescluse et al. (2012) suggest a continuing intraplate deformation between India and Australia, that followed the stress transfer after the Aceh 2004 and Nias 2005 megathrust earthquakes, on preexisting meridian-aligned fault planes of the oceanic lithosphere. Satriano et al. (2012) favor rupture jumping along reactivated NNE–SSW inherited faults that failed sequentially. Reactivation of these faults is also favoured by Andrade and Rajendran (2014). Other models argue that the earthquake pair ruptured two WNW–ESE oriented faults (Duputel et al., 2012;Yue et al., 2012). More complex rupture patterns with varying fault orientations have also been suggested (Meng et al., 2012;Zhang et al., 2012; Ishii et al., 2013;Wei et al., 2013).

Hayes (2012) and Shao et al. (2012) performed finite source inversions from broadband waveforms of P, SH and surface waves and favor a NNE–SSW primary nodal plane of the first, $M_w = 8.6$, event but the second option was not excluded. As to the centroid moment tensor (CMT), there are inconsistencies in routine agency solutions, see Table 1 (the first event) and 2 (the second event), respectively. One can see that the differences among these agency solutions are remarkable. These strike-slip earthquakes generated strong horizontal motions and the M_{rr} component contributes about only 10% to the scalar moment M_0. So, the inverted signal from the body and surface waves is less sensitive to the M_{rr} component than to the other moment tensor components. We assume the trace of the CMT to be zero, and thus only two diagonal components remain independent. The $M_{\phi\phi}$ components seem to be robust in the presented inversion and the question arises whether the remaining diagonal terms can be better constrained by an independent observation.

In this study we demonstrate that the observations of the radial free-oscillations can substantially improve the constraint on the diagonal CMT elements because the radial modes are generated only by the moment tensor component M_{rr}. However, the situation is complicated by the fact that the time difference between the events was only ~124 min and, therefore, we must deal with the M_{rr} components of both earthquakes simultaneously to explain the radial mode ${}_0S_0$ and ${}_1S_0$ oscillations observable for several weeks. It results in systematic trade-off that will be analyzed in detail.

* Corresponding author.
E-mail address: eliskazabranova@centrum.cz (E. Zábranová).

http://dx.doi.org/10.1016/j.pepi.2016.10.001
0031-9201/

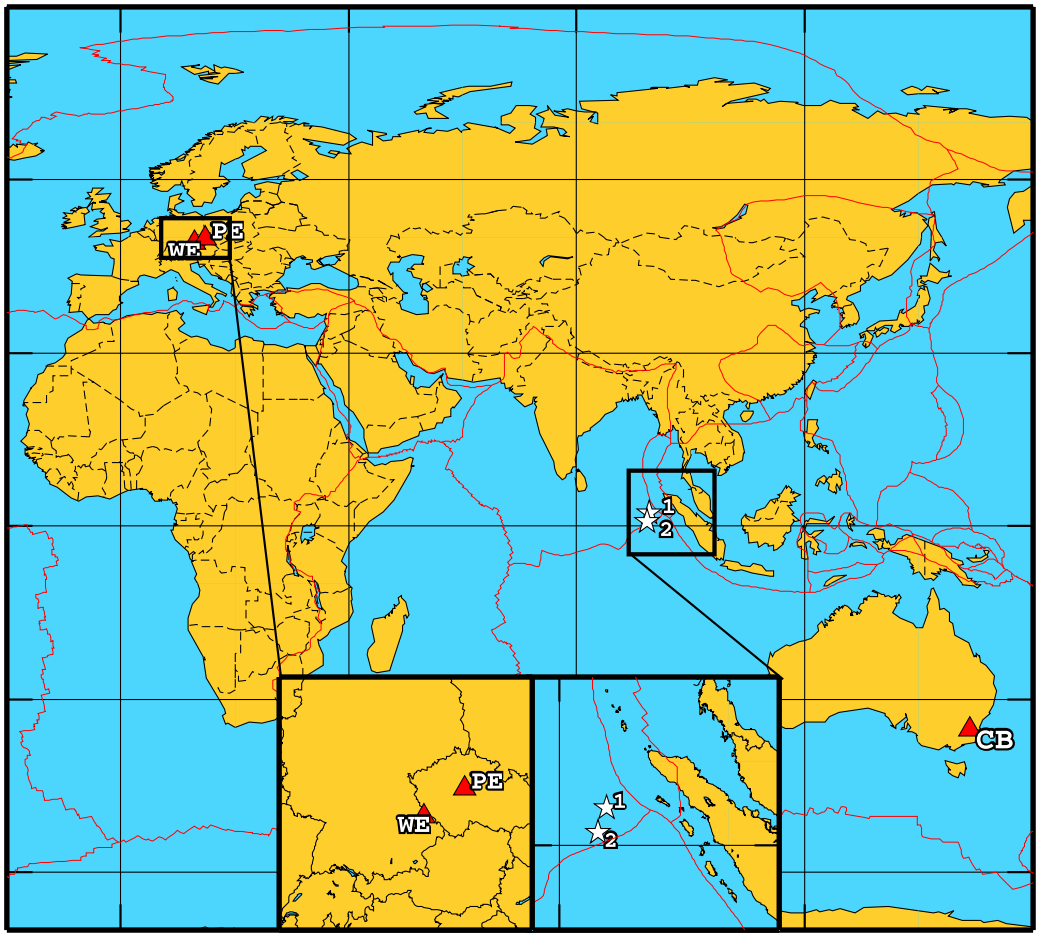

Fig. 1. Locations of the stations Pecný (PE), Canberra (CB) and Wettzell (WE) and epicentres of the two studied earthquakes. The plate boundaries were adopted from Bird (2003).

Table 1
M8.6: April 11, 2012 Sumatra earthquake agency solutions; Global CMT solution (PS1), USGS CMT solution (PS2), USGS Wphase solution (PS3). http://earthquake.usgs.gov/archive/product/phase-data/usp000jhh2/us/1415324847888/quakeml.xml http://www.emsc-csem.org/Earthquake/mtfull.php?id=261636.

	Latitude	Longitude	Depth [km]	Centroid time	M_0 [10^{21} Nm]
PS1	2.24 N	92.78E	40.0	08:39:29.8	9.0
PS2	2.24 N	93.10E	40.0	08:39:32.6	8.5
PS3	2.25 N	92.87E	25.0		9.0

[10^{21} Nm]	M_{rr}	$M_{\theta\theta}$	$M_{\phi\phi}$	$M_{r\theta}$	$M_{r\phi}$	$M_{\theta\phi}$
PS1	1.36	−5.91	4.55	−3.96	0.46	−6.15
PS2	0.40	−5.39	4.98	1.74	−1.57	−6.31
PS3	1.25	−5.99	4.74	1.34	−0.63	−7.03

Table 2
M8.2: April 11, 2012 Sumatra earthquake agency solutions; Global CMT solution (PS1*), USGS CMT solution (PS2*), USGS Wphase solution (PS3*). http://earthquake.usgs.gov/archive/product/phase-data/usp000jhjb/us/1415324848136/quakeml.xml http://www.emsc-csem.org/Earthquake/mtfull.php?id=261684.

	Latitude	Longitude	Depth [km]	Centroid time	M_0 [10^{21} Nm]
PS1*	0.76 N	92.25E	53.7	10:43:37.4	2.5
PS2*	0.92 N	92.49E	43.0	10:43:50.3	2.2
PS3*	0.77 N	92.45E	16.0		3.9

[10^{21} Nm]	M_{rr}	$M_{\theta\theta}$	$M_{\phi\phi}$	$M_{r\theta}$	$M_{r\phi}$	$M_{\theta\phi}$
PS1*	0.59	−1.67	1.08	−1.08	−0.46	−1.89
PS2*	0.45	−1.30	0.85	0.21	−0.84	−1.63
PS3*	−1.18	0.18	1.00	−0.92	−1.33	−3.38

2. Method

The acceleration of a spherically symmetric, anelastic Earth model corrected for ellipticity and rotation at a receiver located at $\mathbf{x}_r(r_r, \vartheta_r, \varphi_r)$, that is excited by a source situated at $\mathbf{x}_s(r_s, \vartheta_s, \varphi_s)$, is given by a superposition of spheroidal and toroidal modes,

$$\mathbf{a}(\mathbf{x}_r, \mathbf{x}_s, t) = \sum_{\mathbf{k}} \mathbf{A}_{\mathbf{k}}(\mathbf{x}_r, \mathbf{x}_s) \cos(\omega_{\mathbf{k}} t) \exp\left(-\frac{\omega_{\mathbf{k}} t}{2Q_{\mathbf{k}}}\right). \quad (1)$$

The coefficients $\mathbf{A}_{\mathbf{k}}(\mathbf{x}_r, \mathbf{x}_s)$ depend on a source-receiver geometry and are linearly related to the moment-tensor $\mathbf{M}$; $\omega_{\mathbf{k}}$ and $Q_{\mathbf{k}}$ are angular frequencies and quality factors of the modes, respectively. The subscript $\mathbf{k}$ represents a multiindex determining the type of a mode (spheroidal or toroidal), the angular degree ℓ, the order m and the overtone number n. Relation between the generated signal at a chosen receiver and the moment tensor is linear. If more sources need to be taken into account, the signal is calculated for each source separately (with a time shift corresponding to an original-time shift) and the resultant signal is obtained simply by adding all individual signals.

If we consider only a part of the response caused by radial (spheroidal, degree-zero) modes for a spherical, non-rotating model, we can directly determine the coefficient $\mathbf{A}_n(\mathbf{x}_r, \mathbf{x}_s)$ of a mode ${}_nS_0$ (Dahlen and Tromp, 1998, Section 10.3),

$$\mathbf{A}_n(r_r, r_s) = \frac{U_n(r_r)}{4\pi}\left[M_{rr}U_n'(r_s) + (M_{\theta\theta} + M_{\phi\phi})\frac{U_n(r_s)}{r_s}\right]\mathbf{e}_{\mathbf{r}}, \quad (2)$$

where the eigenfunctions U_n and their radial derivatives U_n' depend only on the radial coordinate r; M_{rr}, $M_{\theta\theta}$ and $M_{\phi\phi}$ are diagonal components of the centroid moment tensor $\mathbf{M}$. The spherical harmonic degree zero has no lateral variation, i.e., motion is purely vertical, and hence the dependence on colatitude and longitude disappears.

If we assume that the isotropic component of the source is negligible i.e., $M_{rr} = -(M_{\theta\theta} + M_{\phi\phi})$, the acceleration of a device on the Earth's surface ($r_r = a$) caused by the radial modes depends exclusively on one component of the moment tensor, M_{rr}, and on the depth of the centroid,

$$\mathbf{A}_n(a, r_s) = \frac{U_n(a)}{4\pi}\left(1 + \frac{2g}{\omega_n^2 a}\right)M_{rr}\left(U_n'(r_s) - \frac{U_n(r_s)}{r_s}\right)\mathbf{e}_{\mathbf{r}}, \quad (3)$$

where g is an unperturbed gravity acceleration at the surface and the term $(U_n(a)2g/\omega_n^2 a)$ represents the free-air gravity correction due to the radial displacement of the device, (e.g. Dahlen and Tromp, 1998). Note that we ignore perturbations of gravitational potential due to mass redistributions since in the case of radial displacements on a sphere they are non-zero only inside the sphere.

We calculate the eigenfrequencies ω_n and eigenfunctions U_n for the spherical equivalent-rock PREM (Dziewonski and Andersen, 1981), where the upper 3-km water layer is replaced by a 1.2-km-thick rock-layer with the same mass, using our pseudospectral finite-difference matrix-eigenvalue approach (Zábranová et al., 2009). The code was tested for the degenerate case of the non-rotating PREM against the Mineos software package (Masters, 2010) and used in our previous studies, e.g., Zábranová et al. (2012) and Zábranová and Matyska (2014). Corrections due to the rotation and ellipticity in this degree-zero case leads only to a slight shift of the mode frequencies, so formulas (1)–(3) can still be used because each radial mode consists just of one singlet (Dahlen and Tromp, 1998), and coupling with other modes is negligible (Davis et al., 2005). Rosat et al. (2007) showed that for a three-dimensional rotating elliptic Earth model, the difference between theoretically predicted minimum and maximum amplitudes of the ${}_0S_0$ mode is as small as 2%. Moreover, the amplitude spectra of ultra-low-frequency modes are not very sensitive to 3-D structures (Lentas et al., 2014) and thus the spherical approximation with corrections to ellipticity and rotation is sufficient. We used the quality factors of radial modes determined by Zábranová et al. (2012) from data after the 2010 Maule and 2011 Tohoku earthquakes.

3. Data

The best superconducting-gravimeter observations are less noisy than long-period seismometers in the frequencies below 1 mHz (Hinderer, 2011) and they are thus suitable for analyses of the Earth's gravest normal modes. In order to study the radial normal modes, we need unperturbed records at least one month long (radial modes are weak but damped slowly as they have high quality factors, e.g. Zábranová et al., 2012) with high signal/noise ratio. We dealt with second-sampled records from eleven stations and excluded records that are too noisy or contain gaps, steps and/or various other disturbances affecting the spectra like local weak earthquakes. Finally, we have used only four records from the stations Pecný (PE), Canberra (CB) and Wettzell (W3,W4), see Fig. 1.

The raw gravity data were corrected for atmospheric effects using locally recorded atmospheric pressure data and a standard barometric admittance of -3 nm/s^2/hPa (Hinderer et al., 2007). We applied a high-pass Butterworth filter (above 0.1 mHz) to remove local tides and a Hann taper to 450- and 170-h time series in the case of the ${}_0S_0$ and ${}_1S_0$ mode, respectively. Then using the Fourier transform we get the vertical acceleration amplitude and phase spectra that are shown in Fig. 2. It is visible that the amplitude spectral peaks from the individual stations agree within ±10%, which is later considered as the amplitude uncertainty estimate.

4. Results

4.1. Forward modeling

In order to improve the signal/noise ratio, we assume that excitation is almost independent of source-station horizontal geometry and in the time domain we arithmetically averaged the records mentioned in the previous section, i.e., no specific weightening of the records was taken into account. Fig. 3 shows the vertical acceleration amplitude and phase spectra of the radial modes ${}_0S_0$ and ${}_1S_0$ of this averaged data signal and compare it with the synthetic signals generated by point-source solutions provided by the Global CMT solutions (PS1 + PS1*), USGS CMT solutions (PS2 + PS2*) and USGS Wphase solutions (PS3 + PS3*) that are presented in Tables 1 and 2; the solutions without asterisks correspond to the first event and those with asterisk are for the second event. Note that the isotropic component of these published solutions is zero, i.e., in agreement with the assumption that is used in our methodology described above.

Global CMT solutions are based on least-squares inversion of long-period ($T > 45$ s) body-wave seismograms and very-long-period ($T > 135$ s) surface waves using synthetic seismograms calculated by summation of normal modes for the PREM (Dziewonski and Anderson, 1981) and corrected for the Earth's lateral heterogeneities. Details can be found in (Ekström et al., 2012). The USGS CMT solutions are based on similar inversion of surface waves that are filtered to 130 s $< T <$ 330 s (Polet and Thio, 2011). The USGS Wphase solutions exploit the long period content of the seismic records, 200 s $< T <$ 1000 s, preceding the arrival of the surface waves, which corresponds to the superposition of the first overtones of the Earth normal modes (Duputel et al., 2011, 2012).

The synthetic records were filtered and transformed in the same way as the data. Since the fundamental radial mode ${}_0S_0$ has its period of about 20.5 min, the period of the first overtone ${}_1S_0$ is about 10.22 min and the centroid time difference between the studied

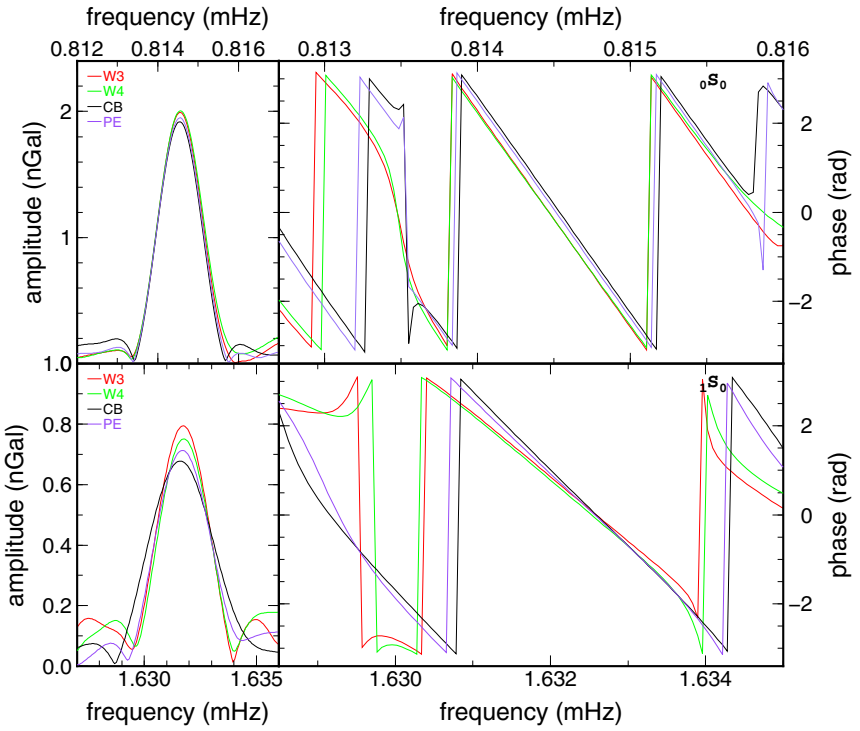

Fig. 2. Vertical acceleration amplitude and phase spectra of the modes $_0S_0$ and $_1S_0$ obtained from the four records registered at the stations Pecný, Canberra and Wettzell. A Hann taper and the Fourier transform were applied to 450- and 170-h time series, respectively.

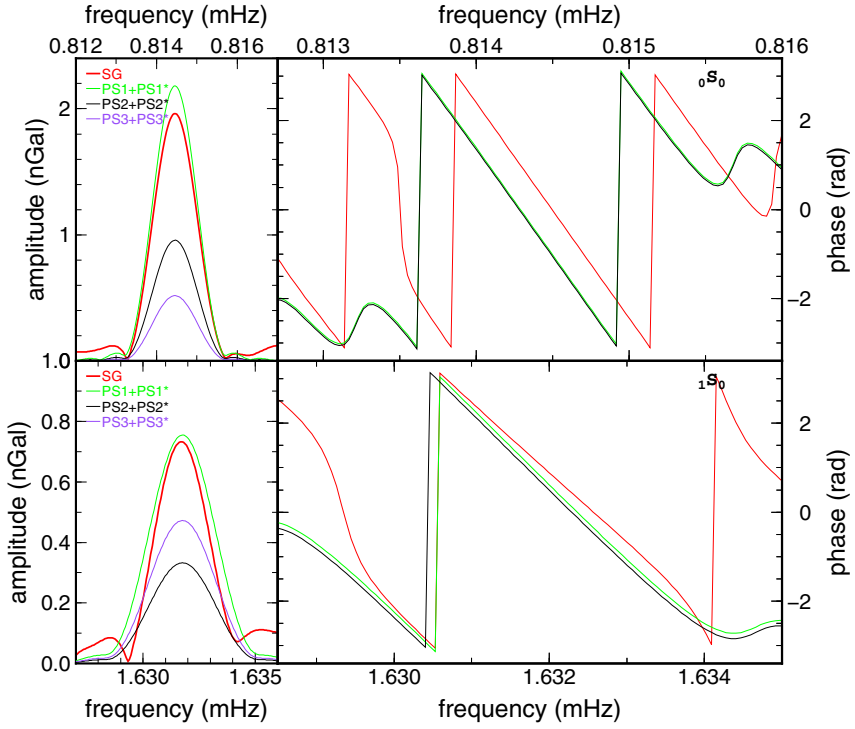

Fig. 3. Vertical acceleration amplitude and phase spectra of the modes $_0S_0$ and $_1S_0$ from the SG data (red) and the three synthetics for the agency point-source solutions, see Tables 1 and 2. A Hann taper and the Fourier transform were applied to 450- and 170-h time series, respectively. (For interpretation of the references to colour in this figure caption, the reader is referred to the web version of this article.)

events is about 124 min, there is only a small phase shift of about 20° for the $_0S_0$ mode and about 45° for the $_1S_0$ mode between the signals from the two studied earthquakes. Therefore, we conclude that the PS3 + PS3* solutions generate too weak signal because M_{rr} components of the two events are of opposite sign. The PS2 + PS2* solutions generate weak signal as well although the M_{rr} components are of the same sign but their values are too low. Only the PS1 + PS1* solutions yield satisfactory fit with the observed data.

It is difficult for us to explain an origin of these inconsistencies; the reason might be that the studied events are of strike-slip character, vertical oscillations were thus relatively weak and, subsequently, their weight in the inversion procedures was low. Moreover, the mode ${}_0S_0$ is out of the frequency band used for the USGS solutions and the weak mode ${}_1S_0$ can hardly influence the Wphase inversion substantially. These radial modes are in the frequency band of the Global CMT solutions and we speculate that this can be the reason why they agree better with our data than the two USGS solution.

4.2. Inverse modeling

We quantify the misfit m as the function of the $M_{rr}^{(1,2)}$ components and the centroid times $t^{(1,2)}$ of both events by

$$m(M_{rr}^{(1)}, M_{rr}^{(2)}, t^{(1)}, t^{(2)}) = \sqrt{\frac{\|A_0^m(M_{rr}^{(1)}, M_{rr}^{(2)}, t^{(1)}, t^{(2)}) - A_0^d\|^2}{\|A_0^d\|^2} + \frac{\|A_1^m(M_{rr}^{(1)}, M_{rr}^{(2)}, t^{(1)}, t^{(2)}) - A_1^d\|^2}{\|A_1^d\|^2}}, \quad (4)$$

where numeral superscripts (subscripts) refer to the event (mode), A^m are the calculated maximal spectral amplitudes of the synthetics and A^d denotes maximal spectral amplitudes obtained from the data. In principle, there is also dependence on source depths but it is almost negligible for source-depth changes of about several km which corresponds to errors in source-depth determination of the studied events. This is the reason why we do not consider them in the misfit definition (4). As the dependence of the calculated amplitude spectra on the changes of the centroid times corresponding to the agency solutions is weak, we first fixed the centroid times and locations on the values given by PS1 for both earthquakes, calculated the synthetic signals and compared them with the data to find admissible values of the M_{rr} components, see Fig. 4.

There is a clear trade-off between both M_{rr} components. If the misfits are calculated separately for the ${}_0S_0$ and ${}_1S_0$ modes (Fig. 4), one can easily recognize from the modal "trade-off curves" that the results for these two cases are self-consistent if the M_{rr} and M_{rr}^* are confined within $\pm 3 \times 10^{21}$ Nm. The key role in reducing the span of preferential solutions is played by the mode ${}_1S_0$. As we deal with the amplitude spectra, there is a point symmetry of the misfit with respect to the point [0,0], because the components $[-M_{rr}, -M_{rr}^*]$ generate the signal with opposite sign to the signal generated by the components $[M_{rr}, M_{rr}^*]$ and, therefore, the amplitude spectra of these two signals are identical. Almost zero phase shifts between the modal oscillations generated by the earthquakes are the cause of elongated "trade-off curves" in Fig. 4; the constraints yielded by a mode with the same phase from the both events would be represented by two parallel lines.

In order to confirm that the uncertainties in determination of centroid times (Tables 1 and 2) are not substantial, we take into account possible variability of the centroid times with a uniform prior distribution and calculate the marginal posterior probability density function (mpdf)

$$\mathrm{mpdf}(M_{rr}^{(1)}, M_{rr}^{(2)}) = \int_{T_1^{(1)}}^{T_2^{(1)}} \int_{T_1^{(2)}}^{T_2^{(2)}} \mathrm{pdf}\, dt^{(1)} dt^{(2)} \quad (5)$$

where

$$\mathrm{pdf} = \frac{\exp(-m^2/2\sigma^2)}{\int_{T_1^{(1)}}^{T_2^{(1)}} \int_{T_1^{(2)}}^{T_2^{(2)}} \int_{M_{rr_1}^{(1)}}^{M_{rr_2}^{(1)}} \int_{M_{rr_1}^{(2)}}^{M_{rr_2}^{(2)}} \exp(-m^2/2\sigma^2) dt^{(1)} dt^{(2)} dM_{rr}^{(1)} dM_{rr}^{(2)}}$$

is the posterior probability density function corresponding to normal prior distribution of dimensionless data errors normalized by amplitude peaks according to eqn. (4) with the relative standard deviation σ (Tarantola, 2005); we apply conservative choice of $\sigma = 0.1$ corresponding to an upper estimate of uncertainties in modal maximal amplitude spectra. The span $T_2^{(1)} - T_1^{(1)}$ of the centroid times of the first event was 48 s centered about 8:39:08 UTC. According to the Wphase analysis of Duputel et al. (2012), the first event ($M_w = 8.6$) can be decomposed into two subevents ($M_w = 8.5$ and $M_w = 8.3$) with the centroid-time shift of the main subevent towards the origin time (8:38:37 UTC). Our time interval thus covers uncertainties of centroid times. Similarly, the span $T_2^{(2)} - T_1^{(2)}$ of the centroid times of the second event was also 48 s centered about 10:43:36 UTC. The considered span of M_{rr} was $\pm 5 \times 10^{21}$ Nm for both events. In principle, we could also calculate the mpdf for the centroid times $t^{(1)}$ and $t^{(2)}$ by integrating the pdf over the components $M_{rr}^{(1)}$ and $M_{rr}^{(2)}$. We performed synthetic tests but the results were very sensitive to changes of the synthetic

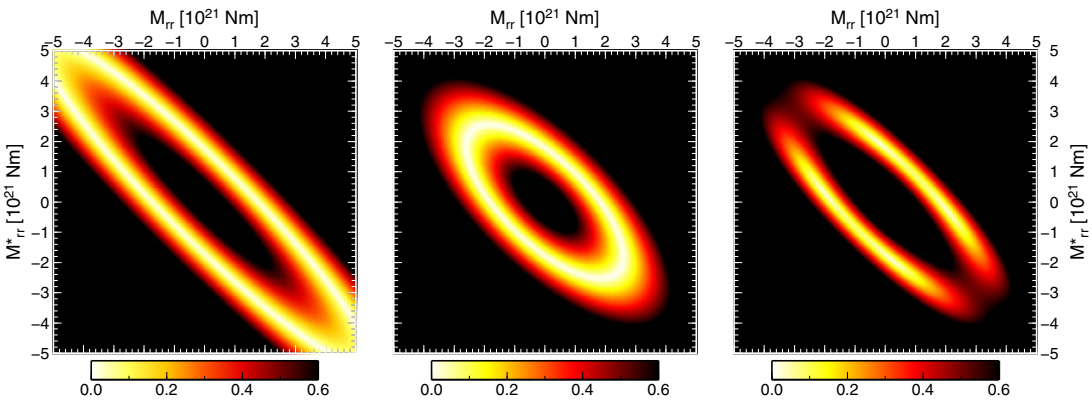

Fig. 4. Constraints on the M_{rr} components of the 2012 Sumatra double-event for 40 km centroid depths; relative misfit of spectral amplitudes calculated separately for L_2-norms of the modes ${}_0S_0$ (left panel), ${}_1S_0$ (middle panel), and for the joint signal from these two modes (right panel) are presented.

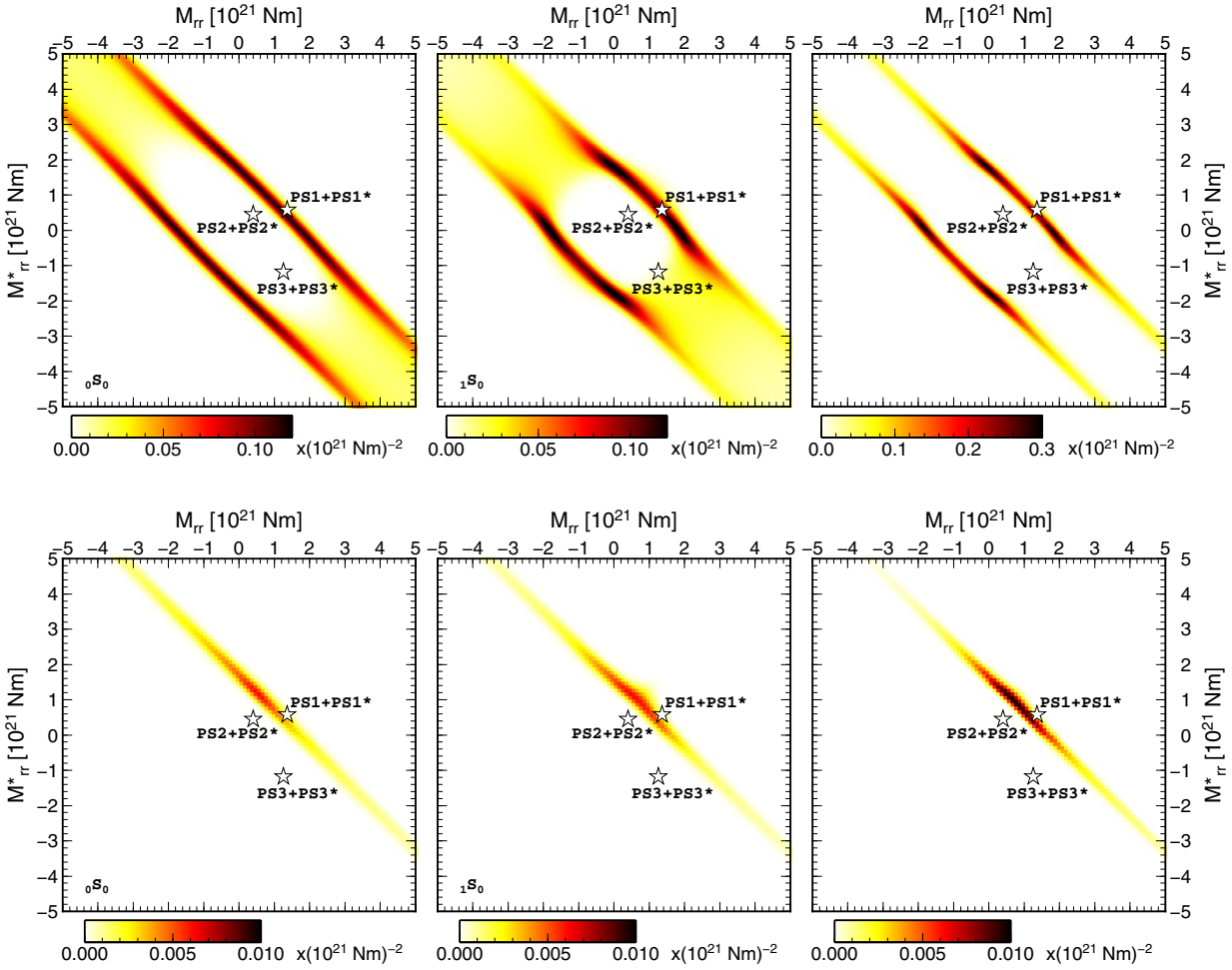

Fig. 5. The mpdf calculated separately for the amplitude spectra (upper panels) and complex spectra (lower panels) of the modes ${}_0S_0$ (left panels), ${}_1S_0$ (middle panels), and for the joint signal from these two modes (right panels). Stars denote published point-source solutions (PS1, PS2 and PS3, see Tables 1 and 2).

source components and maxima of the mpdf did not correspond to synthetic centroid times, which could lead to misinterpretations. These are the reasons why we focus here only to the mpdf expressed by Eq. (5).

The upper row of the panels in Fig. 5 shows mpdf of the two radial modes calculated for the amplitude spectra. By definition of pdf, it is not surprising that the mpdf maxima are in excellent agreement with misfit minima in Fig. 4 that were calculated for fixed centroid times. It is of interest that the most probable solutions seem to be those preferring negligible M_{rr} component of one of the events in combination with $M_{rr} \sim \pm 2 \times 10^{21}$ Nm of the other event. We also tested various combinations of centroid depths between 20 and 40 km. However, the depth-dependence of the source play negligible role in constraining the M_{rr} components (shifts of the constraint curves are only up to a few percent of 10^{21} Nm) and thus we do not show them here.

Subsequently, the lower row of the panels in Fig. 5 shows mpdf calculated for the complex spectra, where both amplitude and phase information are incorporated, i.e., the misfit m was calculated by means of the formula (4) but for the complex spectra. The ambiguity is suppressed as only the wing of the solutions with prevailing positive M_{rr} components provides the mpdf maxima. (Here we used only the record from Canberra because phase spectra of the mode ${}_1S_0$ obtained from the other records are rather corrupted as seen in Fig. 2.).

5. Conclusion

In the case of the 2012 Sumatra double-event the centroid diagonal components M_{rr} of the routine CMT solutions provided by some agencies substantially differ. It points to a need of a study based on independent data and methods. We have demonstrated that superconducting gravimeter observations of the radial modes ${}_0S_0$ and ${}_1S_0$ play an important role as the differences of the modal synthetic amplitudes calculated for the published USGS solutions are strikingly different from the data. The signal calculated for the Global CMT solutions agrees with the data better. The radial modes can thus be employed to constrain the M_{rr} components of these two earthquakes but there is a sign symmetry of the solutions, if only amplitude spectra of the modes are employed. This ambiguity can be resolved, if phase information is added. Moreover, the resulting trade-off between the M_{rr} components is then relatively small.

Acknowledgments

We thank F. Gallovič for discussion, suggestions and comments and two anonymous reviewers for their constructive reviews. We appreciate the help of V. Pálinkáš who collected the superconducting gravimeter data with second sampling. The data employed in this study were registered by the observatories Mount Stromlo (CB), Pecný (PE) and Wetzell (W3. W4). This research was sup-

ported by the Grant Agency of the Czech Republic (GAČR) under the project No. 14-04372S and the LM2010008 project CzechGeo/EPOS.

References

Andrade, V., Rajendran, K., 2014. The April 2012 Indian Ocean earthquakes: seismotectonic context and implications for their mechanisms. Tectonophysics 617, 126–139. http://dx.doi.org/10.1016/j.tecto.2014.01.024.

Bird, P., 2003. An updated digital model of plate boundaries. Geochem. Geophys. Geosyst. 4, 1027. http://dx.doi.org/10.1029/2001GC000252.

Dahlen, F.A., Tromp, J., 1998. Theoretical Global Seismology. Princeton University Press, Princeton.

Davis, P., Ishii, M., Masters, G., 2005. An assessment of the accuracy of GSN sensor response information. Seismol. Res. Lett. 76, 678–683.

Delescluse, M., Chamot-Rooke, N., Cattin, R., Fleitout, L., Trubienko, O., Vigny, C., 2012. April 2012 intra-oceanic seismicity off Sumatra boosted by the Banda–Aceh megathrust. Nature 490, 240–244.

Duputel, Z., Rivera, L., Kanamori, H., Hayes, G.P., Hirshorn, B., Weinstein, S., 2011. Real-time W phase inversion during the 2011 off the Pacific coast of Tohoku earthquake. Earth Planets Space 63, 535–539.

Duputel, Z., Kanamori, H., Tsai, V.C., Rivera, L., Meng, L.S., Ampuero, J.P., Stock, J.M., 2012. The 2012 Sumatra great earthquake sequence. Earth Planet. Sci. Lett. 351, 247–257. http://dx.doi.org/10.1016/j.epsl.2012.07.017.

Dziewonski, A.M., Andersen, D.L., 1981. Preliminary reference Earth model. Phys. Earth Planet. Inter. 25, 297–356.

Ekström, G., Nettles, M., Dziewonski, A.M., 2012. The global CMT project 2004–2010: Centroid-moment tensors for 13,017 earthquakes. Phys. Earth Planet. Inter. 200–201, 1–9.

Hayes, G., 2012. Preliminary Result of the Apr 11, 2012 Mw 8.6 Earthquake Off the West Coast of Northern Sumatra, http://earthquake.usgs.gov/archive/product/finite-fault/usp000jhh2/us/1429388737785/web/s2012OFF-W-01HAYE.fsp.

Hinderer, J., Crossley, D., Warbuton, R.J., 2007. Gravimetric methods – Superconducting gravity meters. In: Herring T. (Ed.), Treatise on Geophysics. pp. 65–122.

Ishii, M., Kiser, E., Geist, E.L., 2013. M_w 8.6 Sumatran earthquake of 11 April 2012: rare seaward expression of oblique subduction. Geology 41, 319–322. http://dx.doi.org/10.1130/G33783.1.

Lentas, K., Ferreira, A.M.G., Clévédé, E., Roch, J., 2014. Source models of great earthquakes from ultra low-frequency normal mode data. Phys. Earth Planet. Inter. 233, 41–67.

Masters G., 2010. Mineos Package <http://geodynamics.org/cig/software/mineos>.

Meng, L., Ampuero, J.-P., Stock, J., Duputel, Z., Luo, Y., Tsai, V.C., 2012. Earthquake in a maze: compressional rupture branching during the 2012 M_w 8.6. Sumatra Earthquake Sci. 337, 724–726. http://dx.doi.org/10.1126/science.1224030.

Polet, J., Thio, H.K., 2011. Centroid-moment-tensor analysis of the 2011 off the Pacific coast of Tohoku Earthquake and its larger foreshocks and aftershocks. Earth Planets Space 63, 519–523.

Rosat, S., Hinderer, J., 2011. Noise levels of superconducting gravimeters: updated comparison and time stability. Bull. Seismol. Soc. Am. 101, 1233–1241.

Rosat, S., Watada, S., Sato, T., 2007. Geographical variations of the ${}_0S_0$ normal mode amplitude: predictions and observations after the Sumatra-Andaman earthquake. Earth Planets Space 59, 307–311.

Satriano, C., Kiraly, E., Bernard, P., Vilotte, J.-P., 2012. The 2012 Mw 8.6 Sumatra earthquake: evidence of westward sequential seismic ruptures associated to the reactivation of a N-S ocean fabric. Geophys. Res. Lett. 39, L15302. http://dx.doi.org/10.1029/2012GL052387.

Shao, G., Li, X., Ji, C., 2012. Preliminary Result of the Apr 11, 2012 Mw 8.64 sumatra Earthquake, <http://www.geol.ucsb.edu/faculty/ji/bigearthquakes/2012/04/10/sumatra.html>.

Tarantola, A., 2005. Inverse Problem Theory and Methods for Model Parameter Estimation. SIAM, Philadelphia.

Wei, S.J., Helmberger, D., Avouac, J.P., 2013. Modeling the 2012 Wharton basin earthquakes off-Sumatra: complete lithospheric failure. J. Geophys. Res. 118, 3592–3609. http://dx.doi.org/10.1002/jgrb.50267.

Yue, H., Lay, T., Koper, K.D., 2012. En échelon and orthogonal fault ruptures of the 11 April 2012 great intraplate earthquakes. Nature 490, 245–249. http://dx.doi.org/10.1038/nature11492.

Zábranová, E., Hanyk, L., Matyska, C., 2009. Matrix pseudospectral method for elastic tides modeling. In: Holota, P. (Ed.), Mission and Passion: Science. Czech National Committee of Geodesy and Geophysics, Prague, pp. 243–260.

Zábranová, E., Matyska, C., Hanyk, L., Pálinkáš, V., 2012. Constraints on the centroid moment tensors of the 2010 Maule and 2011 Tohoku earthquakes from radial modes. Geophys. Res. Lett. 39, L18302. http://dx.doi.org/10.1029/2012GL052850.

Zábranová, E., Matyska, C., 2014. Low-frequency centroid-moment-tensor inversion from superconducting-gravimeter data: The effect of seismic attenuation. Phys. Earth Planet. Inter. 235, 25–32. http://dx.doi.org/10.1016/j.pepi.2014.06.013.

Zhang, H., Chen, J., Ge, Z., 2012. Multi-fault rupture and successive triggering during the 2012 Mw 8.6 Sumatra offshore earthquake. Geophys. Res. Lett. 39, L22305. http://dx.doi.org/10.1029/2012GL053805.